

# Pixel space convolution for cosmic microwave background experiments

P. Fluxá,<sup>a</sup> M.K. Brewer,<sup>b</sup> R. Dünner.<sup>a</sup>

<sup>a</sup>Instituto de Astrofísica, Pontificia Universidad Católica de Chile ,  
Vicuña Mackenna 4860, Chile

<sup>b</sup>Department of Astronomy, Johns Hopkins University,  
Baltimore MD, USA

E-mail: [pedro@fluxanet.net](mailto:pedro@fluxanet.net), [brewer@astro.umass.edu](mailto:brewer@astro.umass.edu), [rdunner@astro.puc.cl](mailto:rdunner@astro.puc.cl)

**Abstract.** Cosmic microwave background experiments have experienced an exponential increase in complexity, data size and sensitivity. One of the goals of current and future experiments is to characterize the B-mode power spectrum, which would be considered a strong evidence supporting inflation. The signal associated with inflationary B-modes is very weak, and so a successful detection requires exquisite control over systematic effects, several of which might arise due to the interaction between the electromagnetic properties of the telescope beam, the scanning strategy and the sky model. In this work, we present the Pixel Space CONvolver (PISCO), a new software tool capable of producing mock data streams for a general CMB experiment. PISCO uses a fully polarized representation of the electromagnetic properties of the telescope. PISCO also exploits the massively parallel architecture of Graphic Processing Units to provide. This work shows the results of applying PISCO in several scenarios, included a realistic simulation of an ongoing experiment, the Cosmology Large Angular Scale Surveyor.

---

## Contents

<b>1</b>	<b>Introduction</b>	<b>1</b>
<b>2</b>	<b>Coordinates</b>	<b>3</b>
2.1	Definitions	3
<b>3</b>	<b>A polarized model for antennas</b>	<b>4</b>
<b>4</b>	<b>Measuring the sky with polarization sensitive antennas</b>	<b>6</b>
4.1	Continuous case	6
4.2	Pixelated case	6
<b>5</b>	<b>PISCO</b>	<b>7</b>
5.1	General description	7
5.2	Implementation using CUDA	7
5.3	Performance	7
5.4	Future improvements	8
<b>6</b>	<b>Code validation</b>	<b>9</b>
6.1	Point source observations	10
6.1.1	Results	10
6.2	Ideal CMB experiment	10
6.2.1	Description	10
6.2.2	Sky model	11
6.2.3	Scanning strategy	11
6.2.4	Power spectra	11
<b>7</b>	<b>A more realistic CMB experiment</b>	<b>12</b>
7.1	Description of the simulations	12
7.1.1	Sky model	12
7.1.2	Pointing	12
7.1.3	Beamsor model	13
7.1.4	Power spectra and beam transfer function	13
7.2	Results and discussion	13
7.2.1	Pointing mismatch	13
7.2.2	Uneven intra-pixel coverage	14
7.2.3	Beam mismatch	14
<b>8</b>	<b>Conclusion</b>	<b>15</b>
<b>A</b>	<b>Computation of antenna basis coordinates and the co-polarization angle from sky coordinates</b>	<b>18</b>

---

## 1 Introduction

The study of the cosmic microwave background (CMB) in the last few decades has lead to major advances in Cosmology. In particular, the study of the temperature and polarization anisotropy field has allowed us to achieve percent level constraints on cosmological parameters, favoring a universe dominated by cold dark matter plus a cosmological constant ( $\Lambda$ CDM), known today as the standard model of Cosmology (see [17]). Current efforts are mostly focused on the

polarization anisotropy field, as it promises to provide independent constraints on the very early stages of the Universe. At these very first moments, the leading theory predicts that the Universe exponentially expanded nearly 60 e-folds in a process called inflation, becoming the flat, homogeneous and isotropic Universe that we see today. If true, gravitational waves generated by this expansion would have later interacted with the surface of last scatter, leaving a unique imprint in the polarization field which should be observable today.

Electromagnetic radiation from the CMB anisotropy field is nearly 10% polarized. These polarized anisotropies can be modeled as a spin-2 field, which is separable in two orthogonal components: a curl-free component called E-mode, and a divergence-free component called B-mode. In the absence of gravitational waves, the polarization field would contain only E-modes, which would be partially turned into B-modes by gravitational waves acting during the epochs of recombination and reionization. The resulting B-mode field would be one or two orders of magnitude lower than the E-mode signal, being very faint and difficult to measure. Moreover, recent results show that this signal lies below other foreground signals like gravitational lensing distortions induced by the matter distribution and polarized emissions from the interstellar medium (see [2]). Thus, detecting the primordial B-mode signal has become a major technical challenge.

Another source of confusion is experimental systematic effects. The tremendous increase in sensitivity of CMB experiments has brought into play a long list of instrumental and observational effects, which need to be properly incorporated not only into the data reduction process, but into the design of future experiments as well. Because the CMB is an extended signal on the sky it is crucial to characterize the beam, or in the more general case, the polarized antenna response of the telescope. It is also key to model and understand how this response gets convolved with the sky signal, as it may directly affect the scientific results.

Modeling the effect of the telescope beam on scientific results can be done analytically or numerically. For instance, the effect of symmetrical beams with smooth profiles can be analytically accounted for when computing the power spectra of CMB maps (see [15]). The impact of other related systematic effects, like beam mismatch, has also been described in the literature (see [5, 14, 21]). When the beam has more complex features, like sidelobes, numerical methods must be used instead. Several techniques that rely on harmonic space representations of the beam, the sky and the scan strategy have been devised (see [3, 22]). An excellent description of an implementation of this is given in [6]. Another approach is the one followed by FeBeCop (see [13]), which computes an effective beam instead of convolving the sky for every time sample.

In this work, we describe the algorithm and prototype implementation of a new CMB computer simulation code, the Pixel Space CONvolver (PISCO). PISCO has the capability of accounting for arbitrary shaped, time-varying beams and sky models. Polarization properties of the beam are handled following the work presented in [14]. PISCO also exploits the massively parallel architecture of Graphics Processing Units (GPU), via the CUDA, and was designed from scratch to take advantage of HPC environments.

This paper is organized as follows. §2 contains a description of the coordinate system and geometrical transformations used to model an antenna pointing at the sky. §3 presents a brief introduction to antenna theory and describes the methodology that was used to model polarizing properties of an antenna. §4.2 describes the algorithm used by PISCO, as well as a prototype implementation. §6 presents validation tests on the prototype implementation of PISCO. §7 provides an example application of PISCO to the Cosmology Large Angular Scale Surveyor, CLASS ([9]). The paper concludes with a brief discussion of the results obtained in §8.

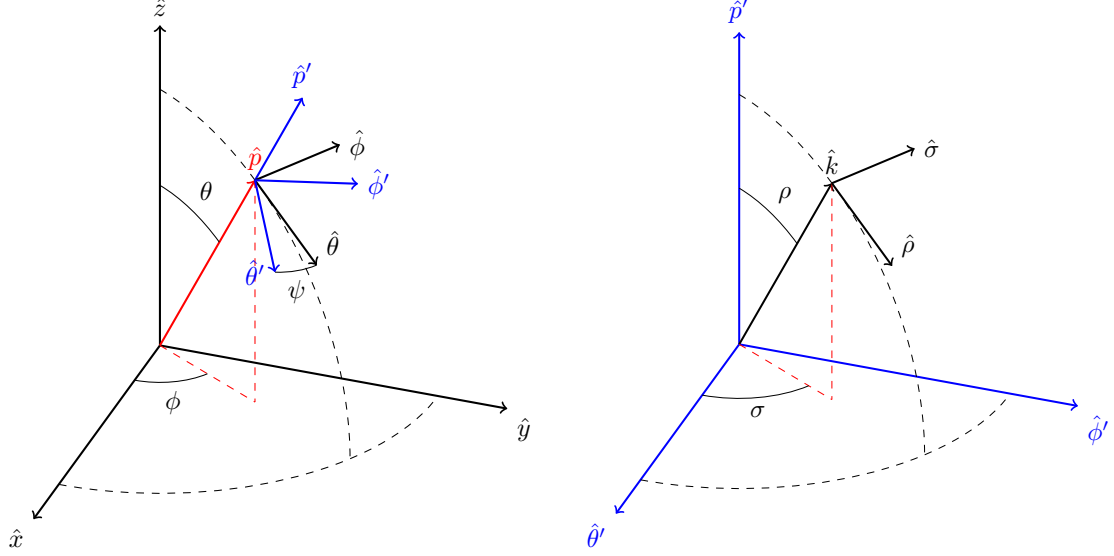


**Figure 1.** Left panel: sky basis. The sky basis is a generic spherical coordinate system.  $\hat{x}$ ,  $\hat{y}$  and  $\hat{z}$  form an orthonormal basis. Unit vector  $\hat{p}$  is defined by its spherical coordinates, co-latitude  $\theta$  and longitude  $\phi$ . Co-latitude increases from the north pole towards the south pole. Longitude increases from west to east. Tangent vectors at  $\hat{p}$ ,  $\hat{\theta}$  and  $\hat{\phi}$ , can be rotated around  $\hat{p}$  by angle  $\psi$  to generate vectors  $\hat{\theta}'$  and  $\hat{\phi}'$ . Note an observer looking towards the sky along  $\hat{p}$  will measure angle  $\psi$  as increasing clockwise from South. Right panel: antenna basis. The antenna basis is another orthonormal basis, very much like the sky basis. A unit vector  $\hat{k}$  is described by  $\rho$  (co-latitude) and  $\sigma$  (longitude). Tangent vectors at  $\hat{k}$  are  $\hat{\rho}$  and  $\hat{\sigma}$ .

## 2 Coordinates

### 2.1 Definitions

Since PISCO performs the convolution of the polarized antenna response with the sky in “real” domain, it makes extensive use of coordinate transformations. These operations can be described by the use of two complementary spherical coordinate systems, which are described in figure 1. The first coordinate system corresponds to the *sky basis*. Unit base vectors of these coordinate system are  $\hat{x}$ ,  $\hat{y}$  and  $\hat{z}$ . For convenience, the antenna pointing in the sky basis will be described as a 3-tuple  $\bar{q}$ , so that an antenna aiming at co-latitude  $\theta_0$  and longitude  $\phi_0$ , with position angle  $\psi_0$  has a pointing

$$\bar{q}_0 = (\theta_0, \phi_0, \psi_0) \quad (2.1)$$

Then the *pointing direction*, denoted by vector  $\hat{p}_0$ , can be expressed as a linear combination of base vectors and spherical coordinates  $(\theta_0, \phi_0)$  via

$$\hat{p}_0 = \sin(\theta_0) \cos(\phi_0) \hat{x} + \sin(\theta_0) \sin(\phi_0) \hat{y} + \cos(\theta_0) \hat{z} \quad (2.2)$$

The vectors  $\hat{\theta}_0$  and  $\hat{\phi}_0$  are computed using

$$\begin{aligned} \hat{\theta}_0 &= \cos(\theta_0) \cos(\phi_0) \hat{x} + \cos(\theta_0) \sin(\phi_0) \hat{y} - \sin(\theta_0) \hat{z} \\ \hat{\phi}_0 &= -\sin(\phi_0) \hat{x} + \cos(\phi_0) \hat{y} \end{aligned} \quad (2.3)$$

These vectors can be used to build a second coordinate system, the *antenna basis*. Given an antenna pointing  $\bar{q}_0$ , the antenna basis base vectors can be written in term of sky basis coordinates as

$$\hat{p}'_0 = \hat{p}_0 \quad (2.4)$$

$$\hat{\theta}'_0 = \cos(\psi_0)\hat{\theta}_0 + \sin(\psi_0)\hat{\phi}_0 \quad (2.5)$$

$$\hat{\phi}'_0 = -\sin(\psi_0)\hat{\theta}_0 + \cos(\psi_0)\hat{\phi}_0 \quad (2.6)$$

In the antenna basis, coordinates analog to sky basis co-latitude and longitude are  $\rho$  and  $\sigma$ , respectively. As in equation 2.2, a vector  $\hat{k}$  can be similarly written in terms of antenna basis coordinates as

$$\hat{k} = \sin(\rho)\cos(\sigma)\hat{\theta}'_0 + \sin(\rho)\sin(\sigma)\hat{\phi}'_0 + \cos(\rho)\hat{p}'_0 \quad (2.7)$$

while vectors analog to the ones described by equation 2.3 are

$$\begin{aligned} \hat{\rho} &= \cos(\rho)\cos(\sigma)\hat{\theta}'_0 + \sin(\rho)\sin(\sigma)\hat{\phi}'_0 - \sin(\rho)\hat{p}'_0 \\ \hat{\sigma} &= -\sin(\sigma)\hat{\theta}'_0 + \cos(\sigma)\hat{\phi}'_0 \end{aligned} \quad (2.8)$$

In many situations, antennas are equipped with polarization sensitive devices. The direction on the sky for which the device has maximum sensitivity to linearly polarized radiation is called co-polarization, and will be denoted by  $\hat{e}_\parallel$ . The perpendicular direction, known as cross-polarization, is denoted by  $\hat{e}_\times$ . Because polarization is defined in the sky basis (see Figure 2), a polarization sensitive antenna must compensate for the apparent rotation of its own polarization basis with respect to the sky. This can be accomplished by rotating the incoming Stokes vector by the angle between  $\hat{e}_\parallel$  and  $\hat{\theta}$ , namely

$$\chi(\rho, \sigma) = \arctan\left(\frac{|\hat{e}_\parallel \times \hat{\theta}|}{\hat{e}_\parallel \cdot \hat{\theta}}\right) \quad (2.9)$$

See Appendix A for details on the definition of co-polarization and cross-polarization that PISCO uses and the computation of  $\chi(\rho, \sigma)$  using spherical trigonometry.

### 3 A polarized model for antennas

The properties of an antenna equipped with detectors that are insensitive to polarization can be fully characterized by its beam. The beam is defined in terms of the antenna angular power density distribution  $U(\rho, \sigma)$  via

$$b(\rho, \sigma) = \frac{U(\rho, \sigma)}{\text{MAX}[U(\rho, \sigma)]} = \frac{U(\rho, \sigma)}{U(0, 0)}. \quad (3.1)$$

From this definition of beam, a standard quantification of an antenna's ability to direct power to a particular region of the sky is given by the beam solid angle  $\Omega$ , calculated as

$$\Omega = \int_{4\pi} b(\rho, \sigma) d\Omega. \quad (3.2)$$

These concepts fully characterize a lossless antenna in the case it is not sensitive to polarization, while modern CMB experiments, aim at measuring E-modes and B-modes. It then becomes necessary to introduce a more general treatment of the antenna, so as to include its polarizing properties.

Many CMB experiments use polarization sensitive bolometers as detection devices, which are pairs of bolometers usually placed at the focus of the optical chain. By construction, each bolometer is more sensitive to a particular orientation of incoming electric fields. This orientation can be parameterized in terms of an angle  $\zeta$ , which is the angle between the orientation of the

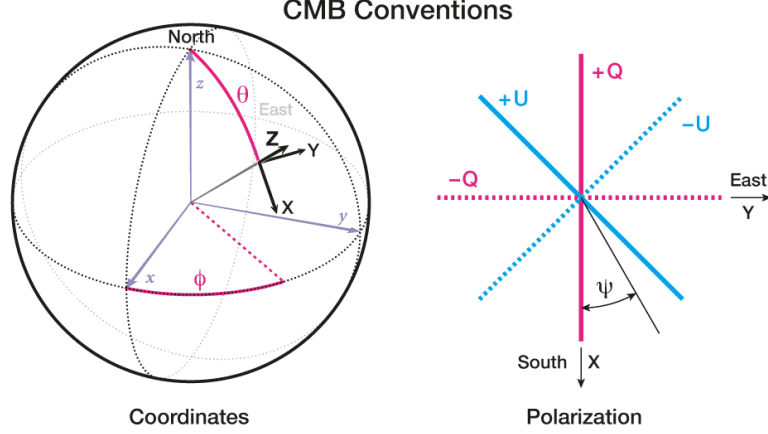


**Figure 2.** Figure showing the convention used for polarization among the CMB community. In this figure,  $z$  is parallel to  $\hat{p}_0$ ,  $x$  is parallel to  $\hat{\theta}$  and  $y$  points along  $\hat{\phi}$ .  $\psi$  is the angle between the antenna “up” direction, and  $x$  ( $\hat{\theta}$ ). The sign conventions of Stokes parameters  $Q$  and  $U$  used by the CMB community are: positive  $Q$  if the polarization vector is aligned with  $\hat{\theta}$  (North-South direction), negative  $Q$  if the polarization vector is aligned with  $\hat{\phi}$  (East-West direction), positive  $U$  is aligned with  $(\pm(\hat{\phi} + \hat{\theta})/\sqrt{2})$  (North/West-South/East direction), and negative  $U$  is aligned with  $(\pm(\hat{\phi} - \hat{\theta})/\sqrt{2})$  (North/East-South/West direction). Note that the right-most panel of this figure corresponds to an observer looking *towards Earth*. Figure source: [LAMBDA website](#)

polarization sensitivity axis of one detector and  $\hat{\theta}'_0$ . Given a polarization sensitive bolometer consisting of a pair of detectors ( $a, b$ ) whose polarization sensitive axes are aligned at angles  $\zeta$  and  $\zeta - 90^\circ$  with respect to the antenna basis unit vector  $\hat{\theta}'_0$ , we can define beam center polarization unit vectors for each detector as

$$\hat{e}_{a,\parallel} = \cos(\zeta)\hat{\theta}'_0 + \sin(\zeta)\hat{\phi}'_0 \quad (3.3)$$

$$\hat{e}_{a,\times} = \sin(\zeta)\hat{\theta}'_0 - \cos(\zeta)\hat{\phi}'_0 \quad (3.4)$$

$$\hat{e}_{b,\parallel} = \sin(\zeta)\hat{\theta}'_0 - \cos(\zeta)\hat{\phi}'_0 \quad (3.5)$$

$$\hat{e}_{b,\times} = -\cos(\zeta)\hat{\theta}'_0 - \sin(\zeta)\hat{\phi}'_0. \quad (3.6)$$

$$(3.7)$$

The polarizing properties of an antenna can be obtained by combining the concept of a beam with the Mueller matrix formalism. Mueller matrices are widely used to quantify the effect that an optical element has on the polarization state of incoming light. This process is modeled by the multiplication of  $4 \times 4$  matrix  $\mathbf{M}$  with a Stokes vector  $S_{\text{in}}$ , such that the Stokes vector of radiation that has interacted with the optical element becomes

$$S_{\text{out}} = \mathbf{M}S_{\text{in}} \quad (3.8)$$

As described in the work of [16] and [14], antennas can be modeled using Mueller matrices. PISCO uses the formalism presented in [14], since it is more suitable to be applied to CMB experiments. We note the original paper names “beam Mueller fields” to this extended definition of a antenna beam. To emphasize the multi-dimensional nature of this mathematical entity, in this work we refer to it as a beam tensor, or *beamsor* for short.

A beamsor can be interpreted as a field of Mueller matrices such that for each direction  $(\rho, \sigma)$ , there is an associated Mueller matrix that quantifies the coupling between the antenna and a Stokes vector coming from  $(\rho, \sigma)$ . We will denote a beamsor by letter  $B = B(\rho, \sigma)$ . At every antenna basis direction,  $B$  is a  $4 \times 4$  matrix in the form

$$B(\rho, \sigma) = \frac{1}{\tilde{\Omega}} \begin{bmatrix} B_{TT} & B_{QT} & B_{UT} & B_{VT} \\ B_{TQ} & B_{QQ} & B_{UQ} & B_{VQ} \\ B_{TU} & B_{QU} & B_{UU} & B_{VU} \\ B_{TV} & B_{QV} & B_{UV} & B_{VV} \end{bmatrix} \quad (3.9)$$

where  $\tilde{\Omega}$  is a normalization factor

$$\tilde{\Omega} = \int_{4\pi} B_{TT}(\rho, \sigma) d\Omega \quad (3.10)$$

and the elements of  $B$  are defined in the work of [14].

## 4 Measuring the sky with polarization sensitive antennas

### 4.1 Continuous case

In order to model the process by which a polarization sensitive detector transforms electromagnetic radiation into current or voltage, we used the formalism described in [10]. In Mueller matrix space, a partially polarized, total power detection device corresponds to the following row-vector

$$D_i(\zeta, \epsilon, s) = \frac{s}{2} [(1 + \epsilon), (1 - \epsilon) \cos(2\zeta), (1 - \epsilon) \sin(2\zeta), 0] \quad (4.1)$$

where  $1 - \epsilon$  is the polarization efficiency,  $s$  is the voltage responsivity of the detector and  $\zeta$  was defined in Section 3 (see Equation 3.7). The process of taking a total power measurement on a Stokes vector  $S^i$  can then be modeled as a dot product

$$d = D_i S^i \quad (4.2)$$

Stokes vector  $S^i$  is, in turn, the convolution between the antenna beamsor and the polarized sky. The complete expression describing the measurement taken by a linearly polarized, total power detector coupled to an antenna pointing along  $\hat{p}$  with position angle  $\psi_0$  becomes

$$d(\bar{q}_0) = \int_{4\pi} D_i(\chi, \epsilon, s) \Lambda_l^i(\chi) B_j^l [\Lambda_m^j(-\chi) S^m] d\Omega \quad (4.3)$$

where  $(i, j) = T, Q, U, V$ , and  $B$  is aligned with  $(\hat{p}, \psi_0)$ . Rotation of the detector polarization basis to the sky basis is carried out using  $\chi$  in the argument to  $D$ , and by  $\Lambda$ , which is a matrix field in the form

$$\Lambda(\chi) = \begin{bmatrix} 1 & 0 & 0 & 0 \\ 0 & \cos(2\chi) & -\sin(2\chi) & 0 \\ 0 & \sin(2\chi) & \cos(2\chi) & 0 \\ 0 & 0 & 0 & 1 \end{bmatrix} \quad (4.4)$$

### 4.2 Pixelated case

In order to calculate the result of equation 4.3 using a computer, we can no longer use continuous distributions, so we need to use pixelated versions of both the beamsor and sky model. Both the sky model  $S$  and beamsor  $B$  must then be transformed into a matrix of  $N_b$  (number of pixels in the beamsor) and  $N_s$  (number of pixels in the sky model) entries, respectively. We will denote the  $k$ -th pixel of the “pixelated” beamsor  $B$  (sky  $S$ ) as  ${}_k B$  ( ${}_k S$ ). With the above in mind, we can write equation 4.3 for the pixelated case as

$$d(\bar{q}_0) = \sum_{k=1}^{N_s} {}_k D_i(\chi, \epsilon, s) {}_k \Lambda_l^i(\chi) {}_k B_j^l {}_k \Lambda_m^j(-\chi) {}_k S^m \quad (4.5)$$

where  $B$  has been properly re-pixelated via interpolation to be aligned with the sky according to  $\bar{q}_0$  using the equations presented in Appendix A.

## 5 PISCO

The **PI**xel **S**pace **CO**nvolver (PISCO) is a tool with the capability of generating synthetic Time Ordered Data (TOD) provided a model for the beamsor, the scanning strategy of the mission and a sky model. In this section, we present a pathfinder implementation of PISCO ( $p$ -PISCO) that exploits the massively parallel architecture of modern GPU systems.

### 5.1 General description

PISCO is the software tool in charge of generating mock TOD given a beamsor, a sky model and a scanning strategy. A diagram showing the general workings of PISCO is shown in Figure 3. PISCO receives as input a sky model in the form of 4 maps representing Stokes parameters  $I, Q, U$  and  $V$ , a beamsor, pointing and focal plane information. PISCO stores the beamsor elements and sky model as HEALPix (see [8]) maps. HEALPix was chosen because it is widely used among the CMB community, and because it naturally handles the closed surface topology of the sphere. HEALPix also provides equal area pixels, which is a desirable feature when computing convolution in pixel space. The focal plane specifications are only needed if multiple detectors are being included in the pointing stream, as PISCO needs the angle  $\zeta$  of each detector to compute equation 4.5. All the inputs are sent to the TOD generation function, which returns the data streams. At this point, the data can either be saved to disk or sent to a map-making code. This last step is preferred as, usually, input-output operations are time consuming. Finally, maps can be analyzed using external tools to calculate the power spectra.

### 5.2 Implementation using CUDA

GPUs allow for substantial acceleration of algorithms that perform a large amount of independent operations. TOD generation using equation 4.5 presents an optimal application case because all operations are independent of each other. In this work, we used the Compute Unified Device Architecture framework from NVIDIA to implement the TOD generation routine. The reader is referred to [20] for an excellent description of CUDA and associated capabilities.

To better understand how the parallelism in 4.5 can be exploited, consider the process of synthesizing  $N_T$  measurements using a CUDA grid of  $B$  blocks and  $T$  threads. Consider each measurement to have an associated pointing  $\bar{q}_t$  with  $t = 0..N_T$ . PISCO performs a double parallelization scheme: the “slow” loop ( $L1$ ) scans the pointing stream and associates every block to a pointing  $\bar{q}_t$ . A second, “faster” loop ( $L2$ ), iterates over a list of pixels, which correspond to sky pixels that are “inside” the beamsor extension. This list of pixels is constructed in advance and then transferred to the GPU.  $L2$  executes  $T$  operations in parallel. Great care was taken to ensure no race conditions arise when multiple threads try to read (write) from (to) the same memory address. As every block executes  $T$  convolution operations in parallel, and the CUDA grid runs  $B$  simultaneous blocks, the parallelism is  $B \times T$ . Furthermore, if  $G$  GPUs are available, the computation can be distributed among them, increasing the parallelism to  $G \times B \times T$ . A graphical description of this process is shown in figure 4.

### 5.3 Performance

A simulation of a realistic CMB experiment (see 7 for more details) took approximately 45 minutes using a node equipped with two Intel Xeon E5-2610 processors (10 physical cores and 20 threads per processor), 256 GB of RAM and one NVIDIA GTX 1080. This simulation generated 1 week of TOD, meaning that PISCO executed around 224 times faster than “real time operation” of the experiment. Unfortunately, measuring performance of the current implementation in FLOPS is a highly nontrivial task: the TOD generation routine performs both integer



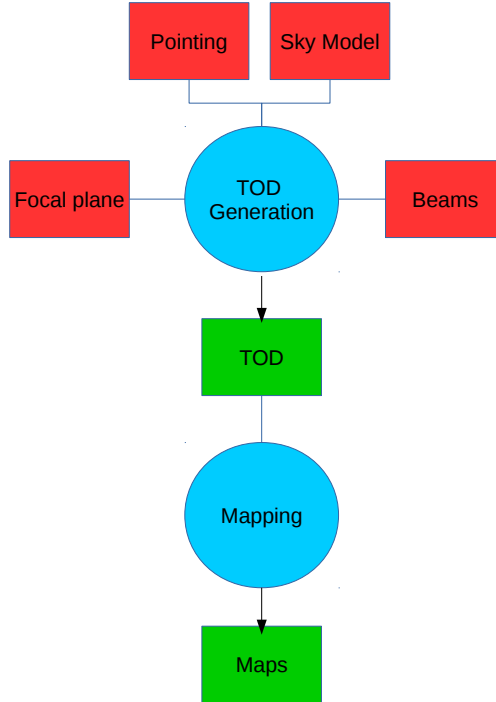


**Figure 3.** Basic flow of a typical PISCO simulation pipeline. Red polygons show the required user input. PISCO uses this input and produces TOD (green polygon). This TOD stream is calculated using equation 4.5 for all pointing directions. TOD can then be sent into a mapper and, finally, to a power spectra estimator tool. PISCO does not compute pointing nor produces maps from TOD by itself; these tasks are left to external programs.

and floating point mathematical operations which are challenging to keep track of. In addition, we were not able to successfully quantify the impact of the memory access pattern caused by having to match beamsor pixels with sky pixels during the convolution step. Nevertheless, and in an effort to provide a comparison basis with other implementations, we claim that this simulation achieved 322560 convolutions per second. It is quite possible for programs like `beamconv` (see [6]) to achieve much higher performance than PISCO for this particular test. It is worth noting, however, that PISCO has a small cost associated to increasing the complexity of the beam, i.e., by adding ghosting, high frequency features (in angular space) and time-dependent beam parameters, or transient events on the sky model, like varying temperature of the ground surrounding the receiver. This makes PISCO a good complement to other software tools that perform similar tasks because, while the computational cost might be larger for “simpler” cases (highly symmetrical beams and no time-dependent effects), the extra cost of adding another layer of complexity is comparatively low.

#### 5.4 Future improvements

The current implementation must calculate the list of sky pixels involved in each convolution, for all pointing directions, before the CUDA routine is launched. Having this list of pixels in memory decreases the available parallelism, as fewer pointing directions can be used at a given time. While the wall-time associated with this operation is modest, the result must be kept in

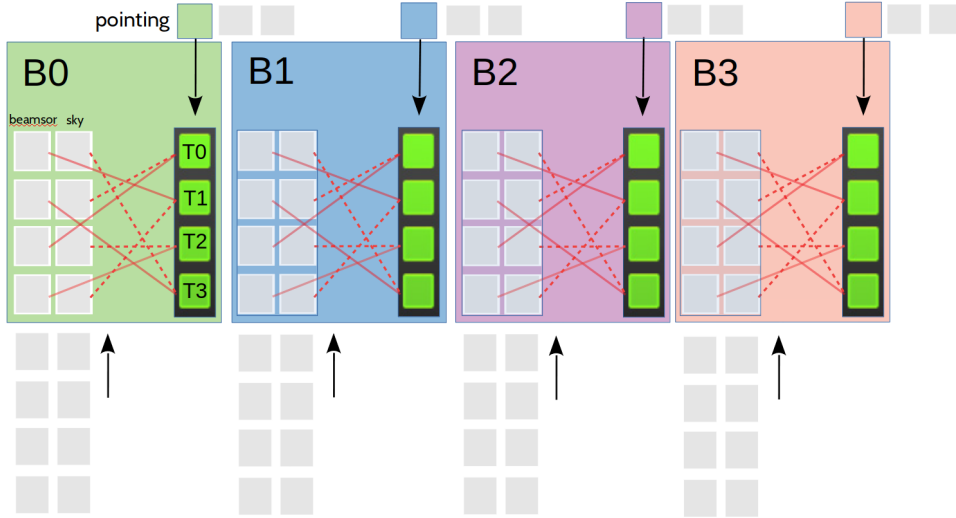


**Figure 4.** Parallelization scheme. This figure shows the case of PISCO executing in 4 blocks ( $B = 4$ ), with four threads per block ( $T = 4$ ). Arrays with beamsor and sky elements are at the bottom. Each block has access to four beamsor and sky pixels (gray boxes inside colored boxes) and one pointing entry (colored small boxes) at a time. Green boxes represent the multiplication process of a single beamsor pixel with a single sky pixel. This includes rotating the sky pixel to the antenna polarization basis, and computing the re-pixelization of  $B$  at the corresponding coordinates. Solid and dotted red lines represent the complex memory access pattern generated by this process. Every thread within a block writes its result to shared memory space. When a thread finishes its computation, it waits until all threads have finished and a reduction on the shared memory space is performed across all blocks. This process is repeated for every pointing. At the end of the procedure, each block has computed the convolution of a beamsor with the sky for a particular pointing, and every shared memory space of the block has the corresponding result. These results are collected into the GPU global memory, which is then transferred back to CPU (host) memory.

memory and transferred to the GPU, so that the associated buffer quickly becomes too large to be held in the VRAM. Currently, PISCO handles this situation by performing the generation of TOD in blocks to avoid memory overflow. In the test machine, computing and transferring the lists of pixels can take up to 13% of the *overall* simulation wall-time. A solution to this problem has already been devised and will be implemented in future releases. Another drawback of the current implementation is the use of global memory to hold the beam tensor elements. Future releases will exploit data locality by making use of the CUDA texture memory pipeline (see [20]). Finally, while the current implementation of PISCO was designed to execute in multiple GPU nodes, significant coding effort is required to provide the user with an easy to use interface. Experiments were performed emulating a multi-node system by making PISCO use all 3 GPUs of the machine. These tests showed an almost linear increase in performance, but more work is required in order to find the knee of the curve between performance and available GPUs.

## 6 Code validation

To validate the correctness of PISCO, we performed two sets of tests: a mock observation of a (polarized) point source and a simulation of an ideal CMB observation. Results from these tests were compared against the `healpy.smoothing` routine, a Python wrapper around HEALPix routines, which calculates the convolution of a polarized sky with a circularly symmetric Gaussian beam in  $a_{\ell m}$  space. For the purposes of this section, we will consider the output of `smoothing` to be exact.

## 6.1 Point source observations

The simulated observation of a polarized point source was accomplished by the following steps

- Build a beamsor without cross-polarization. Every  $B_{ii}$  element corresponds to a circular Gaussian beam with FWHM of  $1.5^\circ$ .
- For simplicity, we used a polarization sensitive bolometer with  $s = 1$  and  $\epsilon = 0$  for both detectors.
- Build a  $I, Q$  and  $U$  skies with a single non-zero pixel at coordinates  $(\theta_k, \phi_k)$ . The Stokes parameters  $S^i = (1, Q, U, 0)$  of the pixel are set such that  $Q^2 + U^2 = 1$  in the polarized cases.
- Set up a raster scan around  $(\theta_k, \phi_k)$  for a detector with  $\zeta = 0$ . Note that, in order to have full polarization coverage, the raster scan is repeated 3 times with angles  $\psi_0 = 0^\circ, 45^\circ, 90^\circ$ .
- Make maps of TOD generated by PISCO.
- Compare the result of applying `smoothing` to the single pixel map using the same beam model.

### 6.1.1 Results

Results from this validation test are shown in figure 5. The results show that the flux is preserved to better than 0.1%. Using a lower NSIDE for the beamsor degrades this considerably. We checked for systematic effects driven by the finite machine precision of the computations, and found that leakage from temperature to polarization is least 10 orders of magnitude below the maximum amplitude of the Stokes I convolved map. PISCO is also able to correctly account for intra-beam variations of the position angle  $\chi$ .

## 6.2 Ideal CMB experiment

### 6.2.1 Description

The simulation of an ideal CMB experiment was accomplished by the following:

- Build a beamsor without cross-polarization. Every  $B_{ii}$  element corresponds to a circular Gaussian beam with FWHM of  $1.5^\circ$ .
- For simplicity, we used a polarization sensitive bolometer with  $s = 1$  and  $\epsilon = 0$  for both detectors.
- Build mock CMB whole sky maps with a tensor-to-scalar ratio  $r = 0.0$ .
- Set up a scanning strategy to visit each pixel center at 3 different position angles  $\psi_0 = 0^\circ, 45^\circ, 90^\circ$ .
- Make maps of TOD generated by PISCO.
- Compare spectra generated from the maps with spectra of the input maps.

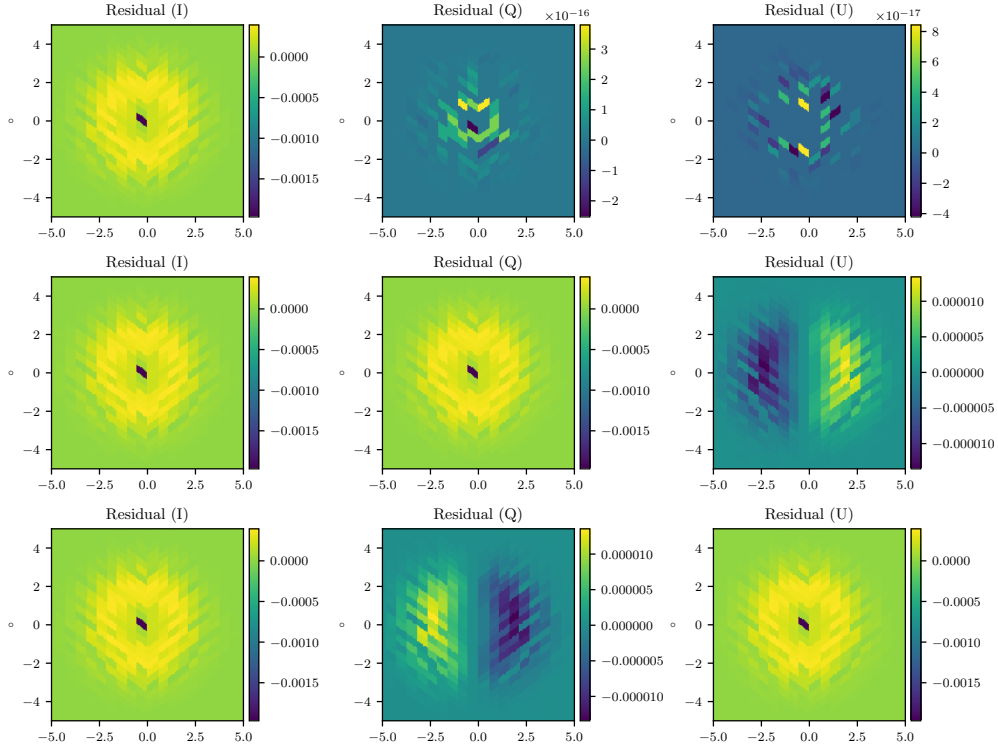


**Figure 5.** Plots showing the result of differencing a map with a point source convolved with a Gaussian beam using `smoothing` and the map generated from PISCO TOD. The input map used HEALPix pixelization with `NSIDE` = 256, while the beamsor resolution was set to `NSIDE` = 1024. The Gaussian profile used for the beamsor had a FWHM of  $1.5^\circ$ . All point sources were located at  $45^\circ$  declination. The color scale is normalized to 1, which is also the amplitude of the source. From top to bottom: residuals for the case of a point source with Stokes vector  $S = (1, 0, 0, 0)$ ,  $S = (1, 1, 0, 0)$  and  $S = (1, 0, 1, 0)$ , respectively.

### 6.2.2 Sky model

The input sky maps were generated using a combination of CAMB (see [11]) to generate  $C_\ell$ , and `synfast` to generate maps from the  $C_\ell$ . The cosmological parameters are consistent with those reported by the Planck satellite collaboration (see [18]). This procedure returns 3 CMB anisotropy maps, one for each Stokes parameter. It is not expected for the CMB to have Stokes  $V$  polarization, so this field was explicitly set to zero. CAMB was configured to return a CMB with no primordial B-modes ( $r = 0$ ) and no lensing, as this last effect is expected to transform E-modes to B-modes. The resulting B-mode power spectrum is effectively zero at all angular scales. No foreground or other sources were added on top of the simulated CMB. All maps use the HEALPix pixelization and were generated at a resolution of `NSIDE` = 128. This restricts the analysis in harmonic space to  $\ell < 384$ .

### 6.2.3 Scanning strategy

The scanning strategy was designed so that every pixel on the sky gets visited exactly three times, each time at a different beam orientation angle. In addition, every pixel was observed at its center, which is an important requirement that ensures the intra-pixel coverage does not affect the estimation of the power spectra at high  $\ell$ . Since only three hits per pixel at different values of  $\chi$  are required to recover the polarization field of the CMB, the scanning was generated for a single detector with a polarization sensitive angle  $\zeta = 0$ .

### 6.2.4 Power spectra

Power spectra were calculated using `anafast`. No further post-processing of the power spectra was needed given that this simulated observation covers the whole sky, and hence no masking

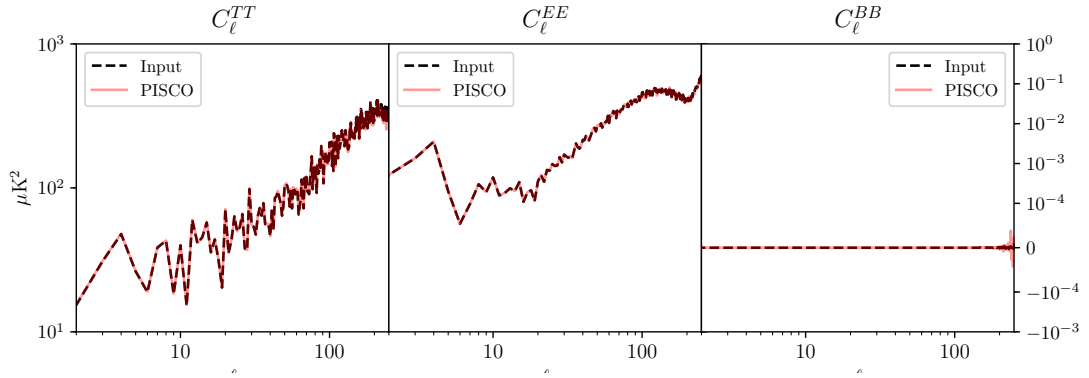


**Figure 6.** Plot showing spectra from PISCO generated TOD (red, solid curve) for the whole sky CMB test (black, dashed curve). Excellent agreement is observed, with no leakage from E-modes to B-modes or from temperature to polarization.

effects arise. The power spectra corresponding to maps that were generated using PISCO TOD were corrected by the equivalent beam transfer function of a circular Gaussian beam of FWHM  $1.5^\circ$ .

## 7 A more realistic CMB experiment

The tests performed in Section 6.2 correspond to an idealized case. In this section, we show results for a simple, but more realistic, application of PISCO. The focus of this section is to demonstrate that the implementation of the model presented in Section 3 is able to reproduce the expected effect of pointing and beam mismatch, which is T to P leakage (see [1]), and uneven intra-pixel coverage, which is divergence in the polarization power spectra at high  $\ell$  (see [19]). We did not include other systematic effects like gain imbalance, detector efficiency, cross-polarization responses and far sidelobes.

### 7.1 Description of the simulations

In this section, we present the procedure and results of a PISCO simulation applied to a more realistic CMB experiment. Since designing such an experiment from scratch is a challenging task, we turned to simulating an ongoing mission, the Cosmology Large Angular Scale Surveyor, CLASS (see [7]). CLASS aims at characterizing the CMB anisotropy field at large angular scales, particularly the power spectra of B-modes and E-modes, looking for evidence of inflation. While the experiment is composed of 4 telescopes, the simulation focuses on the one observing at the lowest frequency (38 GHz), the Q-band receiver. This decision was taken for computational reasons, mainly because Q-band has lower detector count compared to higher frequency receivers. The reader is referred to [9] for a more detailed description of the mission.

#### 7.1.1 Sky model

To generate the maps for this simulation, we followed a similar procedure to the one described in section 6.2.2. The main difference is the addition of an unpolarized CMB, which was used to check for T to P leakage caused by effects that were not present in section ???. All maps use the HEALPix pixelization with an NSIDE parameter of 128.

#### 7.1.2 Pointing

The scanning strategy of CLASS consists of constant elevation scans (CES). Elevation is kept at  $45^\circ$  while the telescope rotates  $720^\circ$  in azimuth at 1 degree per second. This process is repeated for around 18 hours per day. The boresight is rotated from  $-45^\circ$  to  $+45^\circ$  by  $15^\circ$  per day on a weekly schedule. This scanning strategy, in combination with the large CLASS field of view

results in the telescope covering more than 70 percent of the sky every 24 hours. In addition, because of the boresight rotation, only seven days are needed to provide excellent position angle coverage. Boresight rotation is also key to allowing modulation of both  $Q$  and  $U$  signals (see [9]) While CLASS records data 200 times per second, the pointing streams were generated at 20 Hz. This down-sampling factor was selected so as not to produce pixel misses, with the median number of hits per pixel being on the order of thousands. Down-sampling allows for a ten-fold decrease in computation time. Even with this significant reduction, the pointing stream resulted in more than 870 million individual directions.

The equatorial coordinates of every detector were computed from the scanning strategy in horizontal coordinates and the beam center offsets of every detector. Representative beam center offsets of the Q-band receiver were provided by the CLASS collaboration. Two streams were generated by considering detector pairs to have matched or mismatched offsets. The case of matched offsets was simulated by forcing each pair to share the same beam center offsets, which in turn was calculated as the average of the individual pair offsets. Treating the deviation of every offset with respect to the pair average as a Gaussian random error yields an root mean squared mismatch of approximately 5 arc-seconds ( $\approx 0.001^\circ$ ).

### 7.1.3 Beamsor model

The CLASS collaboration provided us with representative main beam parameters. We did not include cross-polarized response of detectors in the beamsors. The main beam parameters correspond to FWHM in the East-West direction ( $\text{FWHM}_x$ ), FWHM in the North-South direction ( $\text{FWHM}_y$ ) and the rotation angle of the major axis of the corresponding elliptical profile. We calculated the degree of beam mismatch from beam parameters following a similar procedure as for the beam center offsets. The root mean square mismatch for  $\text{FWHM}_x$  and  $\text{FWHM}_y$  is  $0.01^\circ$ .

The simplicity of the beams allows for further speed-up in the computation by restricting the convolution to a  $5^\circ$  disc around the beam center. This value was chosen as, for a unit normalized Gaussian beam, a pixel that is  $5^\circ$  away from the centroid of the  $1.5^\circ$  FWHM beam of the CLASS Q band receiver has a value of  $\approx 10^{-14}$ , roughly the limit of double precision arithmetic. All beamsors were pixelated using  $\text{NSIDE} = 512$ . The finite resolution of the beamsor produces an error in the amplitude of simulated TOD that is less than 0.01% compared to analytical estimations, which is consistent with the results described in section 6.

### 7.1.4 Power spectra and beam transfer function

Given that, at present, CLASS only covers  $\approx 75\%$  of the sky, computing the power spectra of simulated maps requires the use of a tool than can handle a sky mask. For this reason, we changed the estimator from **anafast** to **Spice** though the **PolSpice** implementation (see [4]). In addition, the CLASS collaboration provided a realistic sky mask that includes the galactic plane as well as the natural incomplete coverage.

We also need to account for the effect of an elliptical beam on the CMB power spectra. We do this by symmetrizing the beam. This symmetrized beam can be thought of as a low-pass filter in harmonic space (see [15]). We estimated the equivalent beam transfer function of an arbitrary number of elliptical beams by averaging the radial profiles obtained from an analytical integration over  $\phi$  of all of the beams in “real” space, and calculating the harmonic transform of the average profile.

## 7.2 Results and discussion

### 7.2.1 Pointing mismatch

CMB experiments that rely on detector pairs are subject to leakage caused by pointing mismatch. Leakage arises at the map-making stage and is caused by an incomplete cancellation of the Stokes  $I$  term when solving for the individual pixel-covariance matrices. This residual term from the

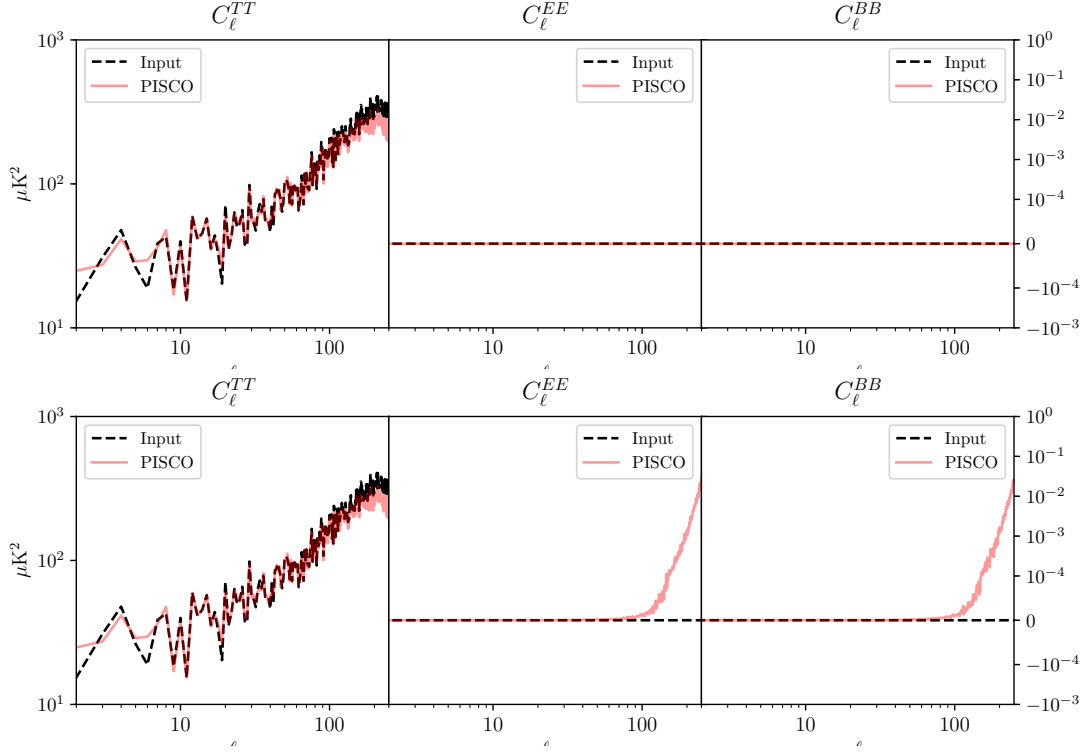


**Figure 7.** Resulting power spectra for a realistic simulation using matched pointing (upper figure), and mismatched pointing (bottom figure). The input CMB was unpolarized. The amplitude of the mismatch was kindly provided by the CLASS collaboration team. Significant leakage from  $TT$  to  $EE$  and  $BB$  power spectra is present for the mismatched pointing case. The spurious signal reaches in the order of  $30 \text{ nK}^2$  at  $\ell = 250$  for both  $EE$  and  $BB$ .

Stokes  $I$  is interpreted by the map-making algorithm as a polarized signal, hence causing the leakage shown in figure 7.

### 7.2.2 Uneven intra-pixel coverage

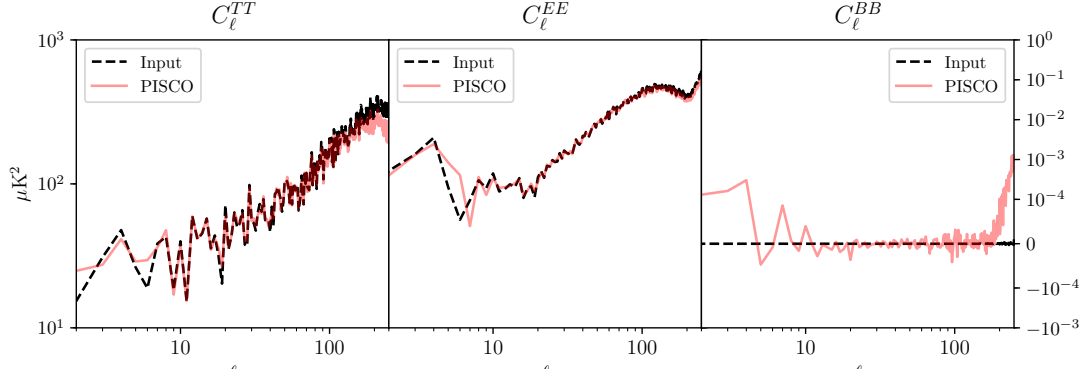
Simulating a CMB experiment using a more realistic scanning strategy can produce another systematic effect at the power spectra level. This source of noise is related to the intra-pixel coverage of the sky. In section 6.2, all pixels were observed exactly at their centers while, in a real experiment, every sample of the TOD “hits” a given pixel at an arbitrary location within it. If the distribution of hits inside a pixel is symmetric with respect to pixel center coordinates, map-making will average all observations and the power spectra from the resulting map will not be affected. However, if this distribution is asymmetric and gradients between pixels are present (recall that pixel space convolution is affected by neighbor pixels) the resulting power spectra may suffer from P to P leakage. This was discussed in more detail in [19].

Figure 8 shows the result of running the realistic simulation using a polarized CMB with matched pointing and it is clear that a spurious signal is present in the B-mode power spectrum. In the upper plot of Figure 7, the same simulation was performed but with an unpolarized CMB as input, the resulting polarized power spectra being consistent with zero. This indicates that the effect of uneven intra-pixel coverage is P to P leakage. We note that this systematic effect is subdominant with respect to the T to P leakage caused by pointing mismatch by roughly a factor of 30.

### 7.2.3 Beam mismatch

The effect of beam mismatch can be thought of as similar to pointing mismatch in that the net effect is to create a spurious polarization signal from the temperature signal. Figure 9 shows





**Figure 8.** Resulting power spectra for the case of matched pointing with uneven intra-pixel coverage using as input a polarized CMB without B-modes. The B-mode power spectrum shows non-negligible amounts of a spurious signal not present in the input power B-mode power spectrum. The spurious B-mode spectrum reaches in the order of  $1 \text{ nK}^2$  at  $\ell = 250$ .

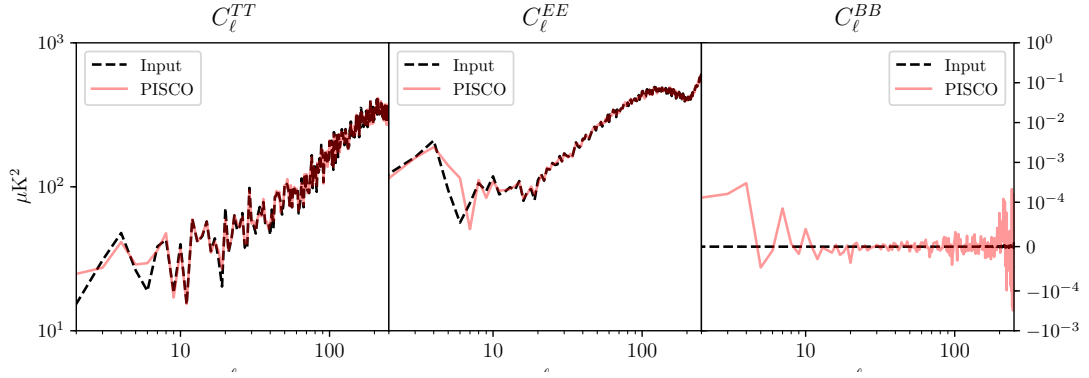


**Figure 9.** Resulting power spectra of a realistic simulation from which the effects of uneven intra-pixel and pointing mismatch have been suppressed. The input CMB was unpolarized, and so the resulting E-mode and B-mode power spectra can only be a result of T to P leakage. The amplitude of the T to P leakage reaches roughly  $0.1 \mu\text{K}^2$  at  $\ell = 250$ .

the resulting power spectra of a simulation with matched pointing, without the effects of uneven intra-pixel coverage. Suppressing the effect of intra-pixel coverage systematics was achieved by forcing the pointing of every detector to aim at its closest sky pixel, for an NSIDE resolution of 128. Results show that PISCO is capable of reproducing the expected systematic effect caused by beam mismatch, which is T to P leakage. We also note that, of all three systematic effects investigated, this produces the largest amount of leakage which, for beam mismatch, reaches approximately  $0.1 \mu\text{K}^2$  at  $\ell = 250$ .

## 8 Conclusion

In this work, we presented a method for simulating the interaction between the electromagnetic properties of an antenna and a polarized sky in the context of CMB experiments. We have also described PISCO, a new computer simulation code that implements this method. PISCO is capable of generating beam-convolved timestreams for arbitrary beams, sky models and scanning strategies and is designed to exploit the natural parallelism in the pixel space convolution algorithm by offloading the computation to the GPU. It is worth mentioning that this implementation can be extended to distribute the calculation among several GPUs. We performed tests applying PISCO to several scenarios: point source convolution, an ideal and a more realistic CMB experiment. This last test was based on the CLASS experiment. The results from these tests indicate that PISCO performs as expected, and is able to reproduce the expected effects



that pointing mismatch, beam mismatch and uneven intra-pixel coverage have on CMB power spectra.

## References

- [1] P. A. R. Ade et al. BICEP2 / Keck Array XI: Beam Characterization and Temperature-to-Polarization Leakage in the BK15 Dataset. 2019.
- [2] BICEP2 Collaboration, Keck Array Collaboration, P. A. R. Ade, Z. Ahmed, R. W. Aikin, K. D. Alexander, D. Barkats, S. J. Benton, C. A. Bischoff, J. J. Bock, R. Bowens-Rubin, J. A. Brevik, I. Buder, E. Bullock, V. Buza, J. Connors, J. Cornelison, B. P. Crill, M. Crumrine, M. Dierickx, L. Duband, C. Dvorkin, J. P. Filippini, S. Fliescher, J. Grayson, G. Hall, M. Halpern, S. Harrison, S. R. Hildebrandt, G. C. Hilton, H. Hui, K. D. Irwin, J. Kang, K. S. Karkare, E. Karpel, J. P. Kaufman, B. G. Keating, S. Kefeli, S. A. Kernasovskiy, J. M. Kovac, C. L. Kuo, N. A. Larsen, K. Lau, E. M. Leitch, M. Lueker, K. G. Megerian, L. Moncelsi, T. Namikawa, C. B. Netterfield, H. T. Nguyen, R. O’Brien, R. W. Ogburn, S. Palladino, C. Pryke, B. Racine, S. Richter, A. Schillaci, R. Schwarz, C. D. Sheehy, A. Soliman, T. St. Germaine, Z. K. Staniszewski, B. Steinbach, R. V. Sudiwala, G. P. Teply, K. L. Thompson, J. E. Tolan, C. Tucker, A. D. Turner, C. Umiltà, A. G. Vieregg, A. Wandui, A. C. Weber, D. V. Wiebe, J. Willmert, C. L. Wong, W. L. K. Wu, H. Yang, K. W. Yoon, and C. Zhang. Constraints on Primordial Gravitational Waves Using Planck, WMAP, and New BICEP2/Keck Observations through the 2015 Season. *PRL*, 121:221301, Nov 2018.
- [3] Anthony Challinor, Pablo Fosalba, Daniel Mortlock, Mark Ashdown, Benjamin Wandelt, and Krzysztof Górski. All-sky convolution for polarimetry experiments. *PRD*, 62:123002, Dec 2000.
- [4] G. Chon, A. Challinor, S. Prunet, E. Hivon, and I. Szapudi. Fast estimation of polarization power spectra using correlation functions. *MNRAS*, 350:914–926, May 2004.
- [5] Santanu Das, Sanjit Mitra, and Sonu Tabitha Paulson. Effect of noncircularity of experimental beam on CMB parameter estimation. *Journal of Cosmology and Astro-Particle Physics*, 2015:048, March 2015.
- [6] Adriaan J. Duivenvoorden, Jon E. Gudmundsson, and Alexandra S. Rahlin. Full-sky beam convolution for cosmic microwave background applications. *arXiv e-prints*, page arXiv:1809.05034, September 2018.
- [7] Thomas Essinger-Hileman, Aamir Ali, Mandana Amiri, John W. Appel, Derek Araujo, Charles L. Bennett, Fletcher Boone, Manwei Chan, Hsiao-Mei Cho, David T. Chuss, Felipe Colazo, Erik Crowe, Kevin Denis, Rolando Dünner, Joseph Eimer, Dominik Gothe, Mark Halpern, Kathleen Harrington, Gene C. Hilton, Gary F. Hinshaw, Caroline Huang, Kent Irwin, Glenn Jones, John Karakla, Alan J. Kogut, David Larson, Michele Limon, Lindsay Lowry, Tobias Marriage, Nicholas Mehrle, Amber D. Miller, Nathan Miller, Samuel H. Moseley, Giles Novak, Carl Reintsema, Karwan Rostem, Thomas Stevenson, Deborah Towner, Kongpop U-Yen, Emily Wagner, Duncan Watts, Edward J. Wollack, Zhilei Xu, and Lingzhen Zeng. CLASS: the cosmology large angular scale surveyor. volume 9153 of *Society of Photo-Optical Instrumentation Engineers (SPIE) Conference Series*, page 91531I, Jul 2014.
- [8] K. M. Górski, E. Hivon, A. J. Banday, B. D. Wandelt, F. K. Hansen, M. Reinecke, and M. Bartelmann. HEALPix: A Framework for High-Resolution Discretization and Fast Analysis of Data Distributed on the Sphere. *APJ*, 622:759–771, April 2005.
- [9] K. Harrington, T. Marriage, A. Ali, J. W. Appel, C. L. Bennett, F. Boone, M. Brewer, M. Chan, D. T. Chuss, F. Colazo, S. Dahal, K. Denis, R. Dünner, J. Eimer, T. Essinger-Hileman, P. Fluxa, M. Halpern, G. Hilton, G. F. Hinshaw, J. Hubmayr, J. Iuliano, J. Karakla, J. McMahon, N. T. Miller, S. H. Moseley, G. Palma, L. Parker, M. Petroff, B. Pradenas, K. Rostem, M. Sagliocca, D. Valle, D. Watts, E. Wollack, Z. Xu, and L. Zeng. The Cosmology Large Angular Scale Surveyor. In *Millimeter, Submillimeter, and Far-Infrared Detectors and Instrumentation for Astronomy VIII*, volume 9914 of *SPIE*, page 99141K, July 2016.
- [10] W. C. Jones, T. E. Montroy, B. P. Crill, C. R. Contaldi, T. S. Kisner, A. E. Lange, C. J. MacTavish, C. B. Netterfield, and J. E. Ruhl. Instrumental and analytic methods for bolometric polarimetry. *AAP*, 470:771–785, August 2007.

- [11] Antony Lewis and Sarah Bridle. Cosmological parameters from CMB and other data: A Monte Carlo approach. *PRD*, 66:103511, 2002.
- [12] A. Ludwig. The definition of cross polarization. *IEEE Transactions on Antennas and Propagation*, 21(1):116–119, January 1973.
- [13] S. Mitra, G. Rocha, K. M. Górski, K. M. Huffenberger, H. K. Eriksen, M. A. J. Ashdown, and C. R. Lawrence. Fast Pixel Space Convolution for Cosmic Microwave Background Surveys with Asymmetric Beams and Complex Scan Strategies: FEBeCoP. *The Astrophysical Journal Supplement Series*, 193:5, March 2011.
- [14] D. O’Dea, A. Challinor, and B. R. Johnson. Systematic errors in cosmic microwave background polarization measurements. *MNRAS*, 376:1767–1783, April 2007.
- [15] L. Page, C. Barnes, G. Hinshaw, D. N. Spergel, J. L. Weiland, E. Wollack, C. L. Bennett, M. Halpern, N. Jarosik, A. Kogut, M. Limon, S. S. Meyer, G. S. Tucker, and E. L. Wright. First-Year Wilkinson Microwave Anisotropy Probe (WMAP) Observations: Beam Profiles and Window Functions. *The Astrophysical Journal Supplement Series*, 148:39–50, September 2003.
- [16] Jeffrey R. Piepmeier, David G. Long, and Eni G. Njoku. Stokes antenna temperatures. *IEEE Transactions on Geoscience and Remote Sensing*, 46(2):516–527, 2008.
- [17] Planck Collaboration, P. A. R. Ade, N. Aghanim, M. Arnaud, M. Ashdown, J. Aumont, C. Baccigalupi, A. J. Banday, R. B. Barreiro, J. G. Bartlett, N. Bartolo, E. Battaner, K. Benabed, A. Benoît, A. Benoit-Lévy, J. P. Bernard, M. Bersanelli, P. Bielewicz, J. J. Bock, A. Bonaldi, L. Bonavera, J. R. Bond, J. Borrill, F. R. Bouchet, F. Boulanger, M. Bucher, C. Burigana, R. C. Butler, E. Calabrese, J. F. Cardoso, G. Castex, A. Catalano, A. Challinor, A. Chamballu, H. C. Chiang, P. R. Christensen, D. L. Clements, S. Colombi, L. P. L. Colombo, C. Combet, F. Couchot, A. Coulais, B. P. Crill, A. Curto, F. Cuttaia, L. Danese, R. D. Davies, R. J. Davis, P. de Bernardis, A. de Rosa, G. de Zotti, J. Delabrouille, J. M. Delouis, F. X. Désert, C. Dickinson, J. M. Diego, K. Dolag, H. Dole, S. Donzelli, O. Doré, M. Douspis, A. Ducout, X. Dupac, G. Efstathiou, F. Elsner, T. A. Enßlin, H. K. Eriksen, J. Fergusson, F. Finelli, O. Forni, M. Frailis, A. A. Fraisse, E. Franceschi, A. Frejsel, S. Galeotta, S. Galli, K. Ganga, T. Ghosh, M. Giard, Y. Giraud-Héraud, E. Gjerløw, J. González-Nuevo, K. M. Górski, S. Gratton, A. Gregorio, A. Gruppuso, J. E. Gudmundsson, F. K. Hansen, D. Hanson, D. L. Harrison, S. Henrot-Versillé, C. Hernández-Monteagudo, D. Herranz, S. R. Hildebrandt, E. Hivon, M. Hobson, W. A. Holmes, A. Hornstrup, W. Hovest, K. M. Huffenberger, G. Hurier, A. H. Jaffe, T. R. Jaffe, W. C. Jones, M. Juvela, A. Karakci, E. Keihänen, R. Keskitalo, K. Kiiveri, T. S. Kisner, R. Kneissl, J. Knoche, M. Kunz, H. Kurki-Suonio, G. Lagache, J. M. Lamarre, A. Lasenby, M. Lattanzi, C. R. Lawrence, R. Leonardi, J. Lesgourgues, F. Levrier, M. Liguori, P. B. Lilje, M. Linden-Vørnle, V. Lindholm, M. López-Caniego, P. M. Lubin, J. F. Macías-Pérez, G. Maggio, D. Maino, N. Mand olesi, A. Mangilli, M. Maris, P. G. Martin, E. Martínez-González, S. Masi, S. Matarrese, P. McGehee, P. R. Meinhold, A. Melchiorri, J. B. Melin, L. Mendes, A. Mennella, M. Migliaccio, S. Mitra, M. A. Miville-Deschênes, A. Moneti, L. Montier, G. Morgante, D. Mortlock, A. Moss, D. Munshi, J. A. Murphy, P. Naselsky, F. Nati, P. Natoli, C. B. Netterfield, H. U. Nørgaard-Nielsen, F. Novello, D. Novikov, I. Novikov, C. A. Oxborrow, F. Paci, L. Pagano, F. Pajot, D. Paoletti, F. Pasian, G. Patanchon, T. J. Pearson, O. Perdereau, L. Perotto, F. Perrotta, V. Pettorino, F. Piacentini, M. Piat, E. Pierpaoli, D. Pietrobon, S. Plaszczyński, E. Pointecouteau, G. Polenta, G. W. Pratt, G. Prézeau, S. Prunet, J. L. Puget, J. P. Rachen, R. Rebolo, M. Reinecke, M. Remazeilles, C. Renault, A. Renzi, I. Ristorcelli, G. Rocha, M. Roman, C. Rosset, M. Rossetti, G. Roudier, J. A. Rubiño-Martín, B. Rusholme, M. Sandri, D. Santos, M. Savelainen, D. Scott, M. D. Seiffert, E. P. S. Shellard, L. D. Spencer, V. Stolyarov, R. Stompor, R. Sudiwala, D. Sutton, A. S. Suur-Uski, J. F. Sygnet, J. A. Tauber, L. Terenzi, L. Toffolatti, M. Tomasi, M. Tristram, M. Tucci, J. Tuovinen, L. Valenziano, J. Valiviita, B. Van Tent, P. Vielva, F. Villa, L. A. Wade, B. D. Wandelt, I. K. Wehus, N. Welikala, D. Yvon, A. Zacchei, and A. Zonca. Planck 2015 results. XII. Full focal plane simulations. *AAP*, 594:A12, Sep 2016.
- [18] Planck Collaboration, P. A. R. Ade, N. Aghanim, M. Arnaud, M. Ashdown, J. Aumont, C. Baccigalupi, A. J. Banday, R. B. Barreiro, J. G. Bartlett, and et al. Planck 2015 results. XIII. Cosmological parameters. *AAP*, 594:A13, September 2016.
- [19] T Poutanen, Giancarlo de Gasperis, Eric Hivon, H Kurki-Suonio, Amedeo Balbi, J Borrill, C Cantalupo, Olivier Doré, E Keihanen, C R. Lawrence, Davide Maino, P Natoli, S Prunet, Radek

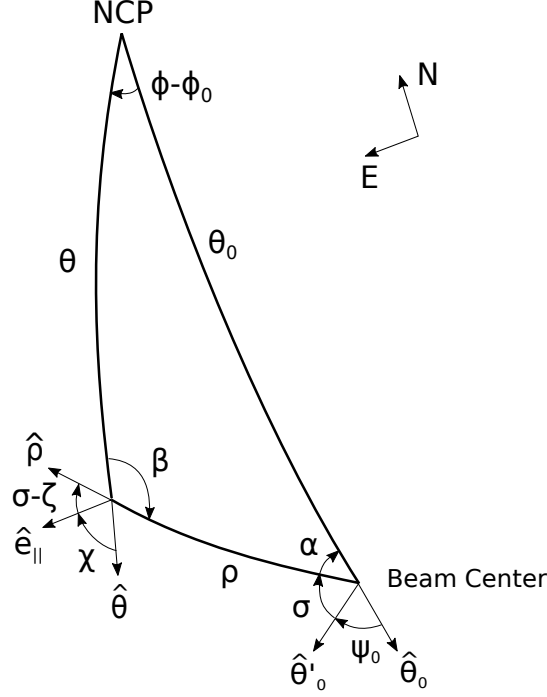


**Figure 10.** Sky and antenna basis coordinates for beam center pointing and off beam center pointing from the viewpoint of an observer looking at the sky. Here **NCP** is the North Celestial Pole and  $\chi$  is the angle between  $\hat{e}_{||}$  and  $\hat{\theta}$  according to Ludwig’s 3rd definition.

Stompor, and Romain Teyssier. Comparison of map-making algorithms for cmb experiments. *Astronomy and Astrophysics*, 01 2005.

- [20] Jason Sanders and Edward Kandrot. *CUDA by example: an introduction to general-purpose GPU programming*. Addison-Wesley Professional, 2010.
- [21] Meir Shimon, Brian Keating, Nicolas Ponthieu, and Eric Hivon. Cmb polarization systematics due to beam asymmetry: Impact on inflationary science. *Phys. Rev. D*, 77:083003, Apr 2008.
- [22] Benjamin D. Wandelt and Krzysztof M. Górski. Fast convolution on the sphere. *PRD*, 63:123002, Jun 2001.

## A Computation of antenna basis coordinates and the co-polarization angle from sky coordinates

For a beam center pointing  $(\theta_0, \phi_0)$ , rotation angle  $\psi_0$  and off beam center pointing  $(\theta, \phi)$  in the sky basis, we can derive the antenna basis coordinates  $(\rho, \sigma)$  and the angle  $\chi$  between  $\hat{e}_{||}$  and  $+Q$  ( $\hat{\theta}$ ) by using spherical trigonometry (see Figure 10). The identities used in this derivation are: the law of cosines, the law of sines and the analogue (or five part) formula.

Defining  $\Delta\phi \equiv \phi - \phi_0$ , the antenna basis coordinate  $\rho$  is given by

$$\rho = \arccos(\cos(\theta)\cos(\theta_0) + \sin(\theta)\sin(\theta_0)\cos(\Delta\phi)) \quad (\text{A.1})$$

Then defining  $\alpha$  as the angle between  $\rho$  and  $\theta_0$ , the antenna basis coordinate  $\sigma$  is given by

$$\sin(\alpha) = \frac{\sin(\theta)\sin(\Delta\phi)}{\sin(\rho)} \quad (\text{A.2})$$

$$\cos(\alpha) = \frac{\cos(\theta)\sin(\theta_0) - \sin(\theta)\cos(\theta_0)\cos(\Delta\phi)}{\sin(\rho)} \quad (\text{A.3})$$

$$\alpha = \arctan\left(\frac{\sin(\theta)\sin(\Delta\phi)}{\cos(\theta)\sin(\theta_0) - \sin(\theta)\cos(\theta_0)\cos(\Delta\phi)}\right) \quad (\text{A.4})$$

$$\sigma = 180^\circ - \psi_0 - \alpha \quad (\text{A.5})$$

Following Ludwig's third definition of cross polarization, substituting  $\sigma + 90^\circ$  for Ludwig's  $\phi$  (see [12]), the unit vectors of co and cross polarization for a detector aligned at an angle  $\zeta$  with respect to the basis vector  $\hat{\theta}'_0$  in the antenna basis are

$$\hat{e}_\parallel = \cos(\sigma - \zeta)\hat{\rho} - \sin(\sigma - \zeta)\hat{\sigma} \quad (\text{A.6})$$

$$\hat{e}_\times = -\sin(\sigma - \zeta)\hat{\rho} - \cos(\sigma - \zeta)\hat{\sigma} \quad (\text{A.7})$$

Thus  $\hat{e}_\parallel$  is offset from  $\hat{\rho}$  by the angle  $\zeta - \sigma$ . Then, defining  $\beta$  as the angle between  $\theta$  and  $\rho$  yields

$$\sin(\beta) = \frac{\sin(\theta_0)\sin(\Delta\phi)}{\sin(\rho)} \quad (\text{A.8})$$

$$\cos(\beta) = \frac{\cos(\theta_0)\sin(\theta) - \sin(\theta_0)\cos(\theta)\cos(\Delta\phi)}{\sin(\rho)} \quad (\text{A.9})$$

$$\beta = \arctan\left(\frac{\sin(\theta_0)\sin(\Delta\phi)}{\cos(\theta_0)\sin(\theta) - \sin(\theta_0)\cos(\theta)\cos(\Delta\phi)}\right) \quad (\text{A.10})$$

$$\chi = \beta + \zeta - \sigma \quad (\text{A.11})$$